The 6th Asian Conference on Multibody Dynamics
August 26-30, 2012, Shanghai, China

Modelling of Joints with Clearance and Friction in Multibody Dynamic Simulation of Automotive Differentials

Geoffrey Virlez
Olivier Brüls
Emmanuel Tromme
Pierre Duysinx
Department of Aerospace and Mechanical Engineering (LTAS)
University of Liège
Liège, 4000, Belgium
Email: {geoffrey.virlez; o.bruls; emmanuel.tromme; p.duysinx}@ulg.ac.be

ABSTRACT

Defects in kinematic joints can sometimes highly influence the simulation response of the whole multibody system within which these joints are included. For instance, the clearance, the friction, the lubrication and the flexibility affect the transient behaviour, reduce the component life and produce noise and vibration for classical joints such as prismatic, cylindric or universal joint. In this work, a new 3D cylindrical joint model which accounts for the clearance, the misalignment and the friction is presented. This formulation has been used to represent the link between the planet gears and the planet carrier in an automotive differential model.

1 INTRODUCTION

Kinematic joints are key components in multibody simulation tools. Most of the time, the joints are represented with idealized models which restrain the motion of the entire system by a set of kinematic constraints. This kind of formulation often considers the joints as perfect rigid elements without any default but has the advantages to be simple to implement and are computationally efficient. However, physical phenomena such as clearance, misalignment, flexibility, friction, lubrication or impact can highly influence the dynamic response of the joints and have a non negligible effect on the accuracy and reliability of the full multibody model. For instance, the modelling of the joints between the suspension arm and the car body with bushing elements strongly influences the vehicle dynamic simulation (Ambrósio and Versissimo, 2009).

The representation of the bodies submitted to the kinematic joints with their actual geometry and their material flexibility properties is without doubt the most accurate way to model any kind of joints. Contact conditions defined between finite element models of the bodies subjected to spherical joints are used in Ambrósio and Versissimo (2009). Such detailed models are able to capture a lot of disruptive factors but they are often quite complex to achieve and they highly increase the computational time.

Other models of joints are at an intermediate level of complexity between the two aforementioned categories. These global joint representations enable to account for some disrupting effects without increasing much the number of degree of freedom. In Bauchau and Rodriguez (2002), the influence of clearance and lubrication is studied for the hinge and spherical joints within the framework of energy preserving and decaying time integration schemes. A planar revolute joint model with clearance based on a continuous contact model is described in Flores (2010). In this paper, the influence of clearance on the dynamic response of a planar slider-crank mechanism is compared to simulations with ideal joints. Similar continuous revolute joint models have been proposed by Ravn (1998) and applied to the simulation of a double pendulum impacting a rigid plate with a study of the noise level generated by impact phenomena. The nonsmooth dynamic approach can also be used to represent kinematic joints with defects, see for example Flores et al (2009) and Dumont and Paoli (2008). This approach often allows to use larger time steps but needs specific integration methods such as time-stepping or event-driven schemes.

The objective of this work is to develop a global model for a cylindrical joint where the clearance, the misalignment and friction force are accounted for (Section 3). A continuous force law is used to model the contact between the pin and the internal cylinder which are represented as rigid bodies. This formulation is based on a restitution coefficient which summarizes the kinetic energy loss at each impact (see Section 3.1). This new joint model has been implemented within the framework of the nonlinear finite element method for multibody systems devel-

oped by Géradin and Cardona (2001) and is briefly presented in Section 2.

The dynamic performance of automotive transmission devices is significantly influenced by the imperfections of kinematic joints. Indeed, these undesirable side effects can introduce discontinuities on the transferred torque and produce vibrations which can affect the security and comfort of the vehicle passengers. The cylindrical joint model described in this paper has been used to model a full TORSEN differential multibody model. The basic working principles of this limited slip differential composed of a planetary gear train are introduced in Section 4.1. Some numerical results illustrating the influence of the misalignment, friction and impacts between the planet gears and the planet carrier on the differential transient response are presented in Section 4.3.

2 FINITE ELEMENT METHOD IN MULTIBODY SYSTEMS DYNAMICS

The nonlinear finite element method for flexible multibody systems (Géradin and Cardona, 2001) enables the modelling of complex mechanical systems composed of rigid and flexible bodies, kinematics joints and force elements. The configuration is represented using absolute nodal coordinates with respect to a unique inertial frame. Hence, there is no distinction between rigid and elastic coordinates which allows accounting in a natural way for many nonlinear flexible effects and large deformations.

The dynamics of a system including holonomic bilateral constraints is described by Eqs. (1-2),

$$\begin{aligned} \boldsymbol{M}(\boldsymbol{q})\,\ddot{\boldsymbol{q}} + \boldsymbol{g}(\boldsymbol{q},\dot{\boldsymbol{q}},t) + \boldsymbol{\Phi}_{\boldsymbol{q}}^{T}(p\boldsymbol{\Phi} + k\boldsymbol{\lambda}) &= \mathbf{0} \quad (1)\\ k\,\boldsymbol{\Phi}(\boldsymbol{q},t) &= \mathbf{0} \quad (2) \end{aligned}$$

where $\boldsymbol{q}$, $\dot{\boldsymbol{q}}$ and $\ddot{\boldsymbol{q}}$ are the generalized displacements, velocities and acceleration coordinates, $\boldsymbol{M}(\boldsymbol{q})$ is the mass matrix, $\boldsymbol{g}(\boldsymbol{q},\dot{\boldsymbol{q}},t) = \boldsymbol{g}^{gyr}(\boldsymbol{q},\dot{\boldsymbol{q}}) + \boldsymbol{g}^{int}(\boldsymbol{q},\dot{\boldsymbol{q}}) - \boldsymbol{g}^{ext}(t)$, with $\boldsymbol{g}^{gyr}$ the vector of the complementary inertia forces, $\boldsymbol{g}^{int}(\boldsymbol{q},\dot{\boldsymbol{q}})$ the vector of the internal forces, e.g. elastic and dissipations forces, and $\boldsymbol{g}^{ext}(t)$ the vector of the external forces. According to the augmented Lagrangian method, the constraint forces are formulated by $\boldsymbol{\Phi}_{\boldsymbol{q}}^{T}(p\boldsymbol{\Phi} + k\boldsymbol{\lambda})$ where $\boldsymbol{\lambda}$ is the vector of Lagrange multipliers related to algebraic constraints $\boldsymbol{\Phi} = \mathbf{0}$; k and p are respectively a scaling and a penalty factor to improve the numerical conditioning.

Equations (1-2) form a system of nonlinear differential-algebraic equations. The solution is evaluated step by step using a second order accurate time integration scheme. For this study, the Chung-Hulbert scheme, which belongs to the family of the generalized α-method, has been used (see Chung and Hulbert (1993), Arnold and Brüls (2007)). At each time step, a system of nonlinear algebraic equations has to be solved using a Newton-Raphson method.

The cartesian rotation vector combined with an updated Lagrangian approach is used for the parametrization of rotations. This choice enables an exact representation of large rotations. The tangent operator, $\boldsymbol{T}(\boldsymbol{\Psi}_{inc})$, enables to compute the material variation of rotations ($\delta\boldsymbol{\Theta}$) from the variation of the incremental cartesian rotation vector ($\delta\boldsymbol{\Psi}_{inc}$).

$$\delta\boldsymbol{\Theta} = \boldsymbol{T}(\boldsymbol{\Psi}_{inc})\;\delta\boldsymbol{\Psi}_{inc} \quad (3)$$

3 JOINT FORMULATION WITH CLEARANCE AND FRICTION FOR A PIN INSIDE A CYLINDER

The formulation of a global joint for the contact between a pin and an inner cylinder is described in this section. The clearance and the friction between these two rigid bodies are taken into account. For specific mechanisms for which the pin tilt is constrained by other parts, the pin can be in contact with the external surface of the hollow cylinder only at one point. We assume that the contact can occur on the top of the cylinder and on the bottom. The contact element developed in this work models the interactions between the cylindrical face of the hollow cylinder and one extremity of the pin. The joint needs to be used twice for each pin: one time for each extremity.

The direction of the contact and friction forces depends on the geometry of the pin at the contact point and can be hardly determined in case of intricate configurations: sharped edge or small fillet radius on the pin external surface for example. The objective of this study is not to analyse detailed phenomena at the contact location but to have a global representation of the related dynamic phenomena. Therefore, in order to have a simple formulation for this 3D contact element, the top of the cylinder has been considered as having a spherical shape (see Fig. 1). This assumption seems reasonable in practical situations where backlash is small and the relative inclination of the pin is limited since the contact point would then remain close to the intersection circle between the sphere and the cylinder. It would thus be close to the physical contact point even if the geometry of the cylinder edge is not precisely represented. The contact force model is managed by a penalty method detailed in Section 3.1. The contact law used is able to model the impacts which occur owing to the clearance between the pin and the cylinder.

This new joint is defined by two physical nodes attached on the two rigid bodies candidate to contact. The node A is located on the axis of the hollow cylinder and the node B is fixed at the center of the top circular face of the pin which is also the center of the contact sphere. The positions and velocities of the twelve absolute nodal coordinates are involved in the expression of this contact element.

A material local frame attached to each body is used in the joint formulation. The triads of orthogonal unit vectors $\{\boldsymbol{e}''_{A_1}, \boldsymbol{e}''_{A_2}, \boldsymbol{e}''_{A_3}\}$ and $\{\boldsymbol{e}''_{B_1}, \boldsymbol{e}''_{B_2}, \boldsymbol{e}''_{B_3}\}$ have their origin fixed respectively at the point A of the hollow cylinder and at the point

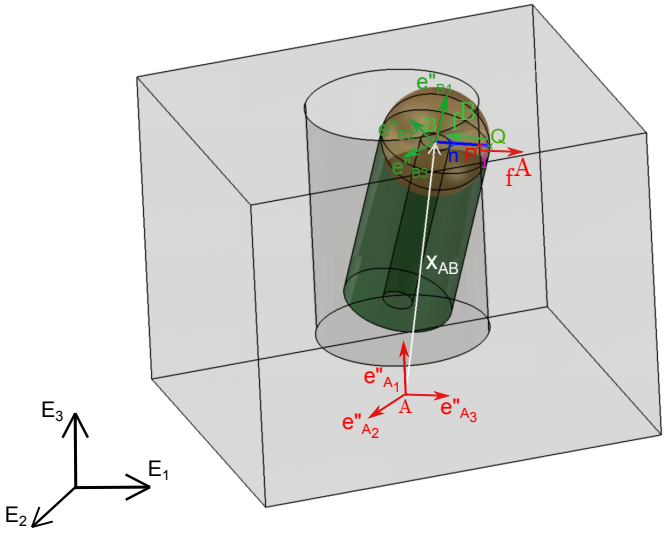

Figure 1. Contact Force

B of the pin. The first triad vectors $\boldsymbol{e}''_{A_1}$ and $\boldsymbol{e}''_{B_1}$ are aligned with the axis of the cylinders. The second triad vectors $\boldsymbol{e}''_{A_2}, \boldsymbol{e}''_{B_2}$ are arbitrary oriented in the plane perpendicular to $\boldsymbol{e}''_{A_1}$ and $\boldsymbol{e}''_{B_1}$. The third unit vectors $\boldsymbol{e}''_{A_3}, \boldsymbol{e}''_{B_3}$ complete the dextrorsum reference frame.

The vectors $\boldsymbol{e}_{A_i}$, $\boldsymbol{e}_{B_i}$ represent the orientation of the two material frames at the initial configuration. In this work, for simplicity the pin and the hollow cylinder are positioned with parallel axis at the initial time. Consequently, the initial orientation is equivalent for the two material frames:

$$\boldsymbol{e}_{A_i} = \boldsymbol{R}_1 \, \boldsymbol{E}_i = \boldsymbol{e}_{B_i} \tag{4}$$

where $\boldsymbol{R}_1$ is the rotation matrix giving the initial orientation of the material frames with respect to the absolute inertial frame $\{\boldsymbol{E}_1, \boldsymbol{E}_2, \boldsymbol{E}_3\}$.

The rotation operators $\boldsymbol{R}_A$,$\boldsymbol{R}_B$ give the orientation of bodies A and B from the initial to the actual configuration.

$$\boldsymbol{e}''_{A_i} = \boldsymbol{R}_A \, \boldsymbol{e}_{A_i} = \boldsymbol{R}_A \, \boldsymbol{R}_1 \, \boldsymbol{E}_i \tag{5}$$

$$\boldsymbol{e}''_{B_i} = \boldsymbol{R}_B \, \boldsymbol{e}_{B_i} = \boldsymbol{R}_B \, \boldsymbol{R}_1 \, \boldsymbol{E}_i \tag{6}$$

The formulation of the normal contact forces and friction forces is described in Sections 3.3 and 3.4 as well as their contributions to the motion equations of the multibody system. The tangent stiffness and damping matrices have been computed analytically but are not given in this paper for the sake of conciseness.

3.1 Continuous contact law

The contact force is defined by the continuous impact model theory developed in Lankarani (1988). This penalty method is based on the Hertz law and uses the penetration (l) as a representation of the local deformation of the two bodies in contact. In addition to the stiffness term, this contact model (Eq. 7) also includes a hysteresis damping term which enables to represent the kinetic energy loss during the impact process. This loss of kinetic energy is described by a restitution coefficient and depends on the shapes and material properties of the colliding bodies as well as their relative velocities. The restitution coefficient e has a value comprised between 0 (plastic contact) and 1 (no energy loss) and can be seen as the absolute value of the ratio of the relative velocity after and before the impact. In order to avoid a jump at the beginning of the contact and tension force at the end, the classical viscous damping term ($c\ \dot{l}$) has been multiplied by l^n.

$$f_c(l, \dot{l}) = k\, l^n + c\, l^n\, \dot{l} \tag{7}$$

with the exponent n equal to 1.5 for circular and elliptic contact areas.

The determination of the contact stiffness parameter k will be discussed in the next section. One way to set the damping parameter c consists in formulating this coefficient as a function of the restitution coefficient. According to the contact configuration, various expressions can be found in the literature, see Lankarani and Nikravesh (1994) for example. The formulation proposed by Flores et al (2011) has been chosen for the definition of the damping parameter c:

$$c = \frac{8\,(1-e)}{5\,e}\,\frac{k}{\dot{l}_s} \tag{8}$$

where $\dot{l}_s$ is the relative normal velocity between bodies at the time of contact establishment. This expression has the advantage to can be used whatever the amount of energy dissipation while most definitions of the damping parameter c are only valid for high values of the restitution coefficient ($e > 0.8$).

3.2 Contact stiffness for sphere to cylinder contact

In order to determine the contact stiffness, the most accurate approach involves a fully flexible finite element model of the two bodies in contact with their actual geometry configuration. The contact stiffness can be obtained by applying a load on one body and using a flexible-flexible contact condition. However, such detailed models can be difficult to elaborate and CPU time expensive. In case of global multibody models, it is preferable to use analytical formulations to compute the contact stiffness. For a sphere in contact with an internal cylinder, a few approximate expressions are available in literature. Puttock and Thwaite (1969) obtain a good approximation of the contact stiffness k (see Eqs. (9-12))

$$k = \frac{2\,\pi}{3(\sigma_1+\sigma_2)} \left(\frac{-\frac{1}{e}\frac{\mathrm{d}E}{\mathrm{d}e}}{A} \right)^{\frac{1}{2}} K^{-\frac{3}{2}} \tag{9}$$

The material parameter σ_i $(i = 1, 2)$ are computed from the Young's modulus E_i and the poisson's ratio ν_i of bodies material.

$$\sigma_i = \frac{1 - \nu_i^2}{E_i} \tag{10}$$

The parameter A is given by the following expression:

$$A = \frac{1}{D_1} - \frac{1}{D_2} \tag{11}$$

where D_1 and D_2 are respectively the diameter of the sphere and the cylinder.

The empirical parameters $-\frac{1}{e}\frac{\mathrm{d}E}{\mathrm{d}e}$ and K are available in lookup tables and are determined according to the ratio $\frac{A}{B}$, defined by:

$$\frac{A}{B} = \frac{\frac{1}{D_1} - \frac{1}{D_2}}{\frac{1}{D_1}} \tag{12}$$

3.3 Normal force

The continuous contact force model described in Section 3.1 does not involve any kinematic constraint. Therefore the contribution of this force element to the motion equations (Eq. 1) of the multibody system is only contained in the term of internal forces, $\boldsymbol{g}^{int}(\boldsymbol{q}, \dot{\boldsymbol{q}})$. The virtual work principle is used in order to formulate the internal force vector of this contact element:

$$\delta W_n = \delta \boldsymbol{x}_P^T \, \boldsymbol{f}^A + \delta \boldsymbol{x}_Q^T \, \boldsymbol{f}^B \tag{13}$$

where $\boldsymbol{x}_P$, $\boldsymbol{x}_Q$ are the position vectors expressed in the absolute frame of the contact point P on the body A and of the contact point Q on the body B (see Figure 1); $\boldsymbol{f}^A$,$\boldsymbol{f}^B$ are the contact forces respectively applied on bodies A and B.

In order to express the virtual displacements $\delta \boldsymbol{x}_P$ and $\delta \boldsymbol{x}_Q$, the points P and Q are considered rigidly fixed on bodies A and B:

$$\begin{aligned} \delta \boldsymbol{x}_P &= \delta \boldsymbol{x}_A + \delta \boldsymbol{\theta}_A \times \boldsymbol{x}_{AP} && (14) \\ \delta \boldsymbol{x}_Q &= \delta \boldsymbol{x}_B + \delta \boldsymbol{\theta}_B \times \boldsymbol{x}_{BQ} && (15) \end{aligned}$$

with $\boldsymbol{x}_{ij} = \boldsymbol{x}_j - \boldsymbol{x}_i$.

The relation between the variation of the spatial angular vector ($\delta\boldsymbol{\theta}$) and the material angular variation vector ($\delta\boldsymbol{\Theta}$) is provided by the initial rotation matrix ($\boldsymbol{R}_1$) and the rotation operators ($\boldsymbol{R}_A$,$\boldsymbol{R}_B$):

$$\begin{aligned} \delta \boldsymbol{\theta}_A &= \boldsymbol{R}_1 \boldsymbol{R}_A \, \delta \boldsymbol{\Theta}_A && (16) \\ \delta \boldsymbol{\theta}_B &= \boldsymbol{R}_1 \boldsymbol{R}_B \, \delta \boldsymbol{\Theta}_B && (17) \end{aligned}$$

In this work, the skew-symmetric matrix $\widetilde{\boldsymbol{i}}$ formed with the components of the vector $\boldsymbol{i}$ is often used to replace the cross products by matrix products ($\boldsymbol{i} \times \boldsymbol{j} = \widetilde{\boldsymbol{i}} \, \boldsymbol{j}$). The virtual displacement of P and Q can be reformulated as:

$$\begin{aligned} \delta \boldsymbol{x}_P &= \delta \boldsymbol{x}_A - \widetilde{\boldsymbol{x}}_{AP} \boldsymbol{R}_1 \boldsymbol{R}_A \, \delta \boldsymbol{\Theta}_A && (18) \\ \delta \boldsymbol{x}_Q &= \delta \boldsymbol{x}_B - \widetilde{\boldsymbol{x}}_{BQ} \boldsymbol{R}_1 \boldsymbol{R}_B \, \delta \boldsymbol{\Theta}_B && (19) \end{aligned}$$

The unit vector $\boldsymbol{n}$ normal to the collision surface between the sphere and the hollow cylinder and aligned with the vector $\boldsymbol{x}_{PQ}$ of maximal indentation l can be defined as:

$$\boldsymbol{n} = \frac{\left(\boldsymbol{I} - \boldsymbol{e}''_{A_1} \boldsymbol{e}''^{\,T}_{A_1}\right) \boldsymbol{x}_{AB}}{\left\| \left(\boldsymbol{I} - \boldsymbol{e}''_{A_1} \boldsymbol{e}''^{\,T}_{A_1}\right) \boldsymbol{x}_{AB} \right\|} \tag{20}$$

where $\boldsymbol{e}''_{A_1}$ is the first axis of the material local frame attached to the node A (see Eqn. 5).

The vector $\boldsymbol{x}_{AP}$ and $\boldsymbol{x}_{BQ}$ can be expressed according to the normal vector $\boldsymbol{n}$ and the distance vector $\boldsymbol{x}_{AB}$:

$$\begin{aligned} \boldsymbol{x}_{BQ} &= r_B \, \boldsymbol{n} && (21) \\ \boldsymbol{x}_{AP} &= \boldsymbol{x}_{AB} + \boldsymbol{x}_{BQ} + \boldsymbol{x}_{QP} && (22) \\ &= \boldsymbol{x}_{AB} + (r_B - l) \, \boldsymbol{n} && (23) \end{aligned}$$

with r_B the radius of the sphere attached at the top of the pin.

The contact forces $\boldsymbol{f}_A$ and $\boldsymbol{f}_B$ are aligned with the normal direction $\boldsymbol{n}$ and their magnitude f_c is given by the contact law (Eq. 7)

$$\boldsymbol{f} = \boldsymbol{f}^B = -\boldsymbol{f}^A = f_c \, \boldsymbol{n} \tag{24}$$

f_c depends on the relative normal deformation (l) and deformation velocity ($\dot{l}$), which are computed according to the following expressions:

$$\begin{aligned} l &= \boldsymbol{x}_{PQ}^T \, \boldsymbol{n} = \boldsymbol{x}_{AB}^T \, \boldsymbol{n} + r_B - r_A && (25) \\ \dot{l} &= \dot{\boldsymbol{x}}_{PQ}^T \, \boldsymbol{n} + \boldsymbol{x}_{PQ}^T \, \dot{\boldsymbol{n}} && (26) \end{aligned}$$

where the second term of $\dot{l}$ is always null because $\boldsymbol{x}_{PQ}$ is parallel to $\boldsymbol{n}$ whereas $\dot{\boldsymbol{n}}$ is perpendicular to $\boldsymbol{n}$. The vector $\dot{\boldsymbol{x}}_{PQ}$ can be obtained owing to the difference of velocity vector of P and Q.

$$\begin{aligned} \dot{\boldsymbol{x}}_P &= \dot{\boldsymbol{x}}_A + \boldsymbol{\omega}_A \times \boldsymbol{x}_{AP} && (27) \\ \dot{\boldsymbol{x}}_Q &= \dot{\boldsymbol{x}}_B + \boldsymbol{\omega}_B \times \boldsymbol{x}_{BQ} && (28) \end{aligned}$$

The spatial angular velocity vector $\boldsymbol{\omega}$ can be transformed to the material angular velocity vector $\boldsymbol{\Omega}$ by:

$$\begin{aligned} \boldsymbol{\omega}_A &= \boldsymbol{R}_1 \boldsymbol{R}_A \, \boldsymbol{\Omega}_A && (29) \\ \boldsymbol{\omega}_B &= \boldsymbol{R}_1 \boldsymbol{R}_B \, \boldsymbol{\Omega}_B && (30) \end{aligned}$$

Finally, the virtual work expression (Eq. 13) can be reformulated as:

$$\delta W_n = \left(\delta \boldsymbol{x}_{AB}^T + \delta \boldsymbol{\Theta}_B^T \boldsymbol{R}_B^T \boldsymbol{R}_1^T \, \widetilde{\boldsymbol{x}}_{BQ} - \delta \boldsymbol{\Theta}_A^T \boldsymbol{R}_A^T \boldsymbol{R}_1^T \, \widetilde{\boldsymbol{x}}_{AP} \right) \boldsymbol{f} \tag{31}$$

The internal force vector $\boldsymbol{g}_n^{int}$ of this normal contact force can be easily obtained by identification of the last expression with the classical virtual work expression for a force element:

$$\delta W = \delta \boldsymbol{q}^T \, \boldsymbol{g}^{int}(\boldsymbol{q}, \dot{\boldsymbol{q}}) \tag{32}$$

where $\boldsymbol{q}$ is the vector of generalized coordinates involved in the force element. For the contact model developed here, the vector

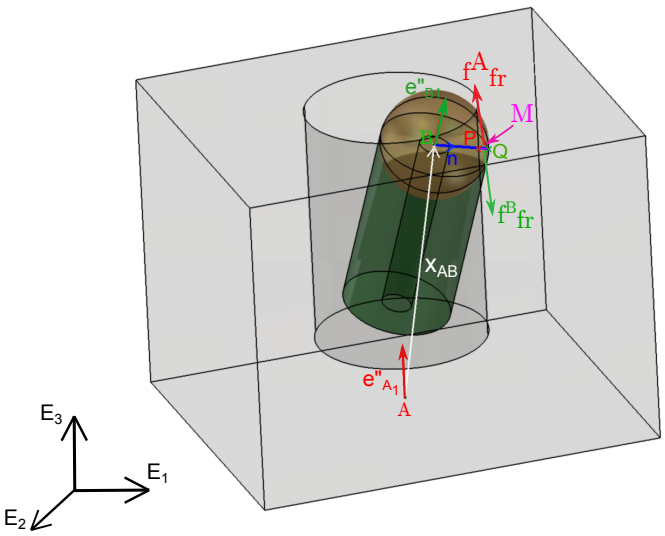

Figure 2. Friction Force

$\boldsymbol{q}$ includes the absolute nodal degree of freedom in translation and rotation of the nodes A and B.

$$\boldsymbol{q} = \begin{Bmatrix} \boldsymbol{x}_A \\ \boldsymbol{\Psi}_{A\ inc} \\ \boldsymbol{x}_B \\ \boldsymbol{\Psi}_{B\ inc} \end{Bmatrix} \tag{33}$$

$$\boldsymbol{g}_n^{int}(\boldsymbol{q}, \dot{\boldsymbol{q}}) = f_c \begin{Bmatrix} -\boldsymbol{n} \\ -\boldsymbol{T}^T(\boldsymbol{\Psi}_{A\ inc}) \boldsymbol{R}_A^T \boldsymbol{R}_1^T \widetilde{\boldsymbol{x}}_{AB}\, \boldsymbol{n} \\ \boldsymbol{n} \\ \boldsymbol{0} \end{Bmatrix} \tag{34}$$

3.4 Friction force

The friction forces $\boldsymbol{f}_{fr}^A$ and $\boldsymbol{f}_{fr}^B$ encountered at the contact between the bodies A and B are considered applied on the point M, located at the middle between the points P and Q (Fig. 2).

The virtual work of the friction forces can be expressed as:

$$\delta W_{fr} = \delta \boldsymbol{x}_M^{A\ T}\, \boldsymbol{f}_{fr}^A + \delta \boldsymbol{x}_M^{B\ T}\, \boldsymbol{f}_{fr}^B \tag{35}$$

where $\delta \boldsymbol{x}_M^A$ is the virtual displacement when M is considered attached to the body A; $\delta \boldsymbol{x}_M^B$ is the virtual displacement when M is considered attached to the body B. By analogy with Eqs. (18-19), the expression of these virtual displacements can be easily obtained:

$$\delta \boldsymbol{x}_M^A = \delta \boldsymbol{x}_A - \widetilde{\boldsymbol{x}}_{AM} \boldsymbol{R}_1 \boldsymbol{R}_A \delta \boldsymbol{\Theta}_A \tag{36}$$

$$\delta \boldsymbol{x}_M^B = \delta \boldsymbol{x}_B - \widetilde{\boldsymbol{x}}_{BM} \boldsymbol{R}_1 \boldsymbol{R}_B \delta \boldsymbol{\Theta}_B \tag{37}$$

The vectors $\boldsymbol{x}_{AM}$ and $\boldsymbol{x}_{BM}$ between the nodes A and B and the application point M of the friction force can be formulated according to $\boldsymbol{x}_{AB}$, $\boldsymbol{n}$, r_B and l

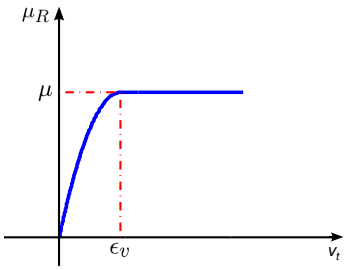

Figure 3. Evolution of the regularized friction coefficient according to the tangential velocity

$$\boldsymbol{x}_{AM} = \boldsymbol{x}_{AP} + \frac{l}{2}\boldsymbol{n} = \boldsymbol{x}_{AB} + \left(r_B - \frac{l}{2}\right)\boldsymbol{n} \tag{38}$$

$$\boldsymbol{x}_{BM} = \boldsymbol{x}_{BQ} - \frac{l}{2}\boldsymbol{n} = \left(r_B - \frac{l}{2}\right)\boldsymbol{n} \tag{39}$$

The friction forces are aligned with the normal vector $\boldsymbol{n}$ but have opposite directions ($\boldsymbol{f}_{fr} = \boldsymbol{f}_{fr}^B = -\boldsymbol{f}_{fr}^A$) and are defined by:

$$\boldsymbol{f}_{fr} = -\mu_R(v_t)\, f_c\, \boldsymbol{t} \tag{40}$$

where f_c is the magnitude of the normal contact force (see Eq. 7), $\boldsymbol{t}$ is the unit tangential vector described hereafter in Eq. (42) and μ_R is the regularized friction coefficient which allows to avoid the large discontinuity when the sign of the relative sliding velocity shifts. Several formulations can be found in the literature for the regularization function and some of them require physical parameters which are quite difficult to determine by numerical simulations or experiments. In this work, a simple quadratic function which depends on v_t, the norm of tangential velocity vector, is used. As depicted in Fig. 3, the regularization tolerance ϵ_v corresponds to the magnitude of the tangential velocity where the regularized friction coefficient μ_R reaches the constant kinetic friction coefficient μ.

$$\mu_R(v_t) = \begin{cases} \mu\left(2\,\dfrac{v_t}{\epsilon_v} - \left(\dfrac{v_t}{\epsilon_v}\right)^2\right) & v_t < \epsilon_v \\ \mu & v_t \geq \epsilon_v \end{cases} \tag{41}$$

The unit tangential vector $\boldsymbol{t}$ can be simply expressed by:

$$\boldsymbol{t} = \frac{\boldsymbol{v}_t}{v_t} \tag{42}$$

where $\boldsymbol{v}_t$ is the vector of tangential velocity at the point M where the friction forces are applied:

$$\boldsymbol{v}_t = \left(\boldsymbol{I} - \boldsymbol{n}\boldsymbol{n}^T\right)\left(\dot{\boldsymbol{x}}_M^B - \dot{\boldsymbol{x}}_M^A\right) \tag{43}$$

$\dot{\boldsymbol{x}}_M^A$ and $\dot{\boldsymbol{x}}_M^B$ are the velocity vectors when the point M is respectively attached to the bodies A and B.

$$\dot{\boldsymbol{x}}_M^A = \dot{\boldsymbol{x}}_A + \boldsymbol{\omega}_A \times \boldsymbol{x}_{AM} \tag{44}$$

$$\dot{\boldsymbol{x}}_M^B = \dot{\boldsymbol{x}}_B + \boldsymbol{\omega}_B \times \boldsymbol{x}_{BM} \tag{45}$$

The virtual work expression of the friction forces can be reformulated as:

$$\delta W_{fr} = \left(\delta \boldsymbol{x}_{AB}^T + \delta \boldsymbol{\Theta}_B^T \boldsymbol{R}_B^T \boldsymbol{R}_1^T \, \widetilde{\boldsymbol{x}}_{BM} - \delta \boldsymbol{\Theta}_A^T \boldsymbol{R}_A^T \boldsymbol{R}_1^T \, \widetilde{\boldsymbol{x}}_{AM} \right) \boldsymbol{f}_{fr} \tag{46}$$

The identification with the equation (32) is straightforward and allows to obtain the vector of internal forces $\boldsymbol{g}_{fr}^{int}$

$$\boldsymbol{g}_{fr}^{int}(\boldsymbol{q}, \dot{\boldsymbol{q}}) = \left\{ \begin{array}{c} -\boldsymbol{f}_{fr} \\ -\boldsymbol{T}^T(\boldsymbol{\Psi}_{A\ inc}) \boldsymbol{R}_A^T \boldsymbol{R}_1^T \widetilde{\boldsymbol{x}}_{AM} \ \boldsymbol{f}_{fr} \\ \boldsymbol{f}_{fr} \\ \boldsymbol{T}^T(\boldsymbol{\Psi}_{B\ inc}) \boldsymbol{R}_B^T \boldsymbol{R}_1^T \widetilde{\boldsymbol{x}}_{BM} \ \boldsymbol{f}_{fr} \end{array} \right\} \tag{47}$$

4 APPLICATION: TORSEN DIFFERENTIAL

4.1 Presentation of the system

The two essential functions of a differential are to transmit the motor torque to the two output shafts and to allow a difference of rotation speed between these two outputs. In a vehicle, this mechanical device is particularly useful in turn when the outer wheels have to rotate quicker than the inner wheels to ensure a good handling. The differential can be used either to divide the drive torque into equal parts acting on the traction wheels of the same axle, or to divide the output torque from the gearbox between the two axles of four-wheels drive vehicles. This second application is often called the transfer box differential or central differential.

The main drawback of a conventional differential (open differential) is that the total amount of available torque is always split between the two output shafts with the same constant ratio. The TORSEN differentials significantly reduce this undesirable side effect. This kind of limited slip differential allows a variable distribution of motor torque depending on the available friction of each driving wheel.

When a TORSEN differential is used, the torque biasing is always a precondition before any difference of rotation speed between the two output shafts. Contrary to viscous coupling, TORSEN (a contraction of Torque-Sensing) is an instantaneous and pro-active process which acts before wheel slip.

The type C TORSEN differential has been fully modeled in this work. As depicted in Fig. 4, this central differential is mainly composed of a epicyclic gear, several thrust washers and a housing in two parts. The friction encountered by the contact between the planet gears and the housing as well as between the gear wheels and the thrust washers is at the origin of the locking effect and torque transfer of TORSEN differentials. This limited slip differential has four working modes which depend on the direction of torque biasing and on the drive or coast situation. According to the considered mode, the gear wheels rub against one or the other thrust washers which can have different friction coefficients and contact surfaces. The locking rate is different for each working mode and is directly related to the total friction torque involved.

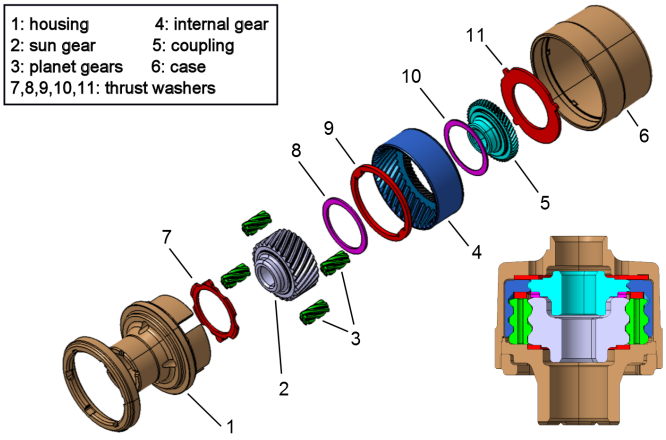

Figure 4. Kinematic diagram, exploded view and cut-away view of type C TORSEN differential

The assembly of planet gears on planet carrier is particular in this mechanical device. Indeed, planet gears are inserted in housing cylindrical cavities without any physical rotational axis. The clearance between crater and planet gear diameters allows planet gears to tilt which involve contact between gear teeth top and crater external surface. The friction occurred by these contacts tends to slow down the relative rotation and significantly contributes to the locking effect. The transient behaviour at the switching time between two working modes is also highly influenced by this specific assembly.

4.2 Model description

The two main kinematic joints needed to model TORSEN differentials are gear pairs and contact conditions. The formulation used to model each gear pair is available for describing flexible gear pairs in 3 dimensional analysis of flexible mechanism. This gear element is developed in Cardona (1995) and it is a global kinematic joint defined between two physical nodes: one at the center of each gear wheel which is represented as a rigid body. Nevertheless the flexibility of the gear mesh is accounted for by a nonlinear spring and damper element inserted along the instantaneous normal pressure line. Several specific phenomena in gear pairs are also included in the model: backlash, mesh stiffness fluctuation, friction between teeth. The displacement and the inclination of the planet gears influence the gear mesh properties. However the mesh misalignment has not been taken into account in this model because the gear pair model used is not able to manage the tilt of the gear wheels. With the gear model used, the gear wheel axis have to remain parallel. However this assumption is acceptable for the type C TORSEN differential since the clearance between the planet gears and the housing is very low ($40\ \mu\mathrm{m}$) and allows only a inclination angle of $0.2°$ for the planet gears inside the housing cavities.

The modeling of contacts between the lateral faces of gear

wheels and the thrust washers have been carried out with a penalty method combined with a squeeze film model of the lubricated oil between the thrust washers and the gear wheels.

A dynamic analysis of the TORSEN differential has been achieved in a previous work (see Virlez et al (2011) for more details) where the connection between the planet gears and the housing were modeled by classical cylindrical joints without clearance. The comparison of the torque distribution ratios provided by the numerical simulation with experimental data permits to globally validate the model. However, with this idealized joint, the stresses and the friction distribution have shown sizable deviations.

In this paper, the 4 cylindrical joints have been replaced by the actual joint model defined in Section 3. In addition to the 8 planet gear/housing joints, the global model also includes 15 rigid bodies, 8 gear pairs, 14 contact elements, and 1 screw joint. The number of generalized coordinates is about 800. The contacts elements developed here as well as the gear pair model introduce non-symmetric terms in the tangent iteration matrix. Therefore a non-symmetric resolution algorithm has been used although it is computationally more expensive.

4.3 Numerical results

In order to study in a simple way the behavior of the new cylindrical joint in the configuration of the TORSEN differential, only a reduced part of the differential has been modeled in a first instance. As depicted in Figure 5, this simple system includes a unique planet gear, the sun gear, the housing and one thrust washer. The sun gear is linked to the housing with a hinge joint and is submitted to a torque linearly increasing from 0 Nm at $t = 0$ s to reach 10 Nm for the period $t = [0.3; 0.5]$ s before decreasing following a linear function to -20 Nm for the period $t = [0.8; 1]$ s. The planet gear is meshing with the sun gear and its axial displacement in the z-axis is constrained by two unilateral contact conditions (one defined with the housing and one defined with the thrust washer). The housing and the thrust washer are clamped to the ground.

The displacement in the $x - y$ plane of the top and bottom face center of the planet gear inside the housing hole is depicted in Fig. 6. At the initial time, the planet gear is located at the center of the housing cavity and their axis are parallel. As soon as a torque is applied on the sun gear, the meshing force tends to increase the gear wheel center distance and the planet gear is deported against the circular face of housing cavity. After the first impact, the planet gear undergoes several rebonds but tends to keep a constant global orientation until the torque applied on the gear wheel changes of direction. At this time, the planet gear quickly moves to negative values of y-axis and also tend to maintain a fixed position after the transient period. Due to the helical gear teeth, the planet gear is tilted during the transient phases, which explains the small differences of trajectory observed on Fig. 6(a) compared to Fig. 6(b).

Figure 7 illustrates the kinetic energy dissipation which is

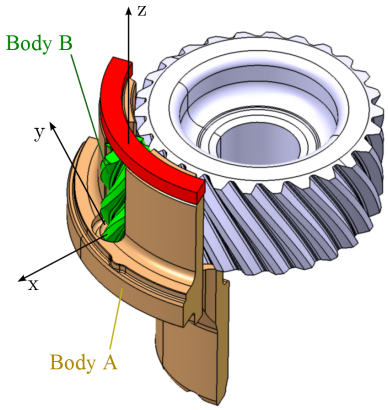

Figure 5. Test model for the new joint in the geometrical configuration of TORSEN differential

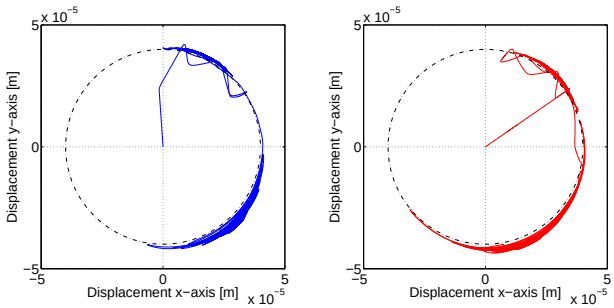

(a) bottom face center (b) top face center

Figure 6. Trajectory of the face center relative to the center of the housing cavity.

taken into account by the contact law (Eq. 7) at each impact. Indeed, the hysteresis loops encircle the amount of energy dissipated owing to the damping term used in the contact force. The areas of these hysteresis loops highly depends on the choice of the restitution coefficient. In this example, this coefficient has been fixed to 0.8, a frequently used value for contacts between two metallic bodies.

Finally, the new cylindrical joint formulation has been introduced in a full TORSEN differential model. For this simulation the same configuration as experimental settings on testrig has been reproduced. A torque is progressively applied on one output shaft whereas the rotation velocity is prescribed on the second output and the housing is clamped on the test bench. Figure 8 depicts the resistant torque which allows to limit the rotation velocity of the sun gear when a 50 Nm torque is applied in 0.1 s on the coupling. The spikes at the beginning of the simulation ($t = [0; 0.02]$ s) are caused by the shocks due to the clearance in the cylindrical joints. The discontinuities observed during the second part of the simulation are due to the contact es-

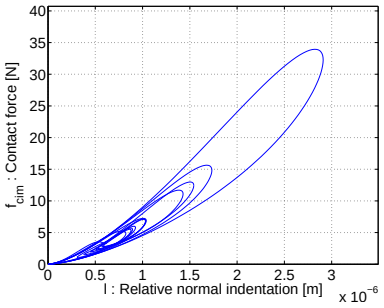

(a) planet gear bottom

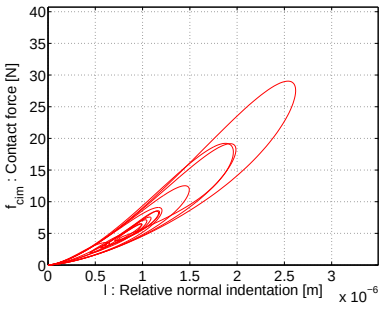

(b) planet gear top

Figure 7. Hysteresis loops of the contact force illustrating the energy dissipation for the first impacts.

tablishment between the gear wheels and the thrust washers. For instance, the friction inherent to the contact between the internal gear and the thrust washer #11 modifies the friction torques in the differential as soon as this unilateral contact is active and explains the step on the curve at $t = [0.07; 0.08]$ s. Although the transient behavior is influenced by the imperfections of the joints, the mean value of the resistant torque is similar to the value obtained when the PG/housing joints are modeled with idealized cylindrics.

5 CONCLUSION

In this paper, a non-ideal cylindrical joint has been presented. This joint model accounts for several imperfections often encountered in mechanical joints: clearance, misalignment, friction and impact forces. The formulation is based on a continuous impact force law to model the contacts between the pin tips and the lateral face of the hollow cylinder. The loss of kinetic energy at each impact is accounted for by a restitution coefficient introduced inside the damping parameter. This new joint has been tested within a TORSEN differential multibody model in order to represent the assembly of the planet gears on the planet carrier. The simulations allow to study the transient response of this epicyclic gear train. However, for this kind of complex industrial system which includes numerous discontinuous and nonlinear phenomena and where the efforts transmitted are high, the continuous contact models require very small time steps ($h \leq 10^{-6}$ s) to insure the convergence of the integration algorithm. The modelling of contacts with nonsmooth techniques may be an alternative to avoid this drawback and permit faster simulation of global multibody systems with non-ideal kinematic joints (see preliminary work in Chen et al (2012)). Furthermore, accurate values for the restitution coefficient and the friction coefficient needed in the joint definition are not easy to determine in some intricate geometrical configurations such as the contact between the gear wheel teeth tip and the cavity in the planet carrier. Detailed models of the contact area could provide more accurate estimation of these physical parameters and will be investigate in a future work.

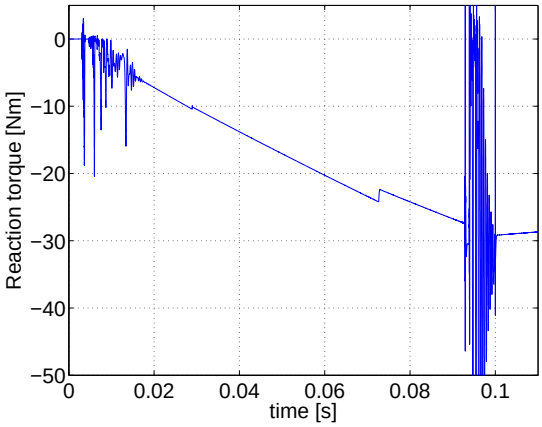

Figure 8. Transient variations of resistant torque on coupling due to clearance and misalignment at the beginning of the simulation.

ACKNOWLEDGMENT

The author, Geoffrey Virlez would like to acknowledge the Belgian National Fund for Scientific research (FRIA) for its financial support.

REFERENCES

Ambrósio J, Versissimo P (2009) Improved bushing models for general multibody systems and vehicle dynamics. msd 22:341–365

Arnold M, Brüls O (2007) Convergence of the generalized-α scheme for constrained mechanical systems. Multibody System Dynamics 18(2):185–202

Bauchau O, Rodriguez J (2002) Modeling of joints with clearance in flexible multibody systems. International Journal of Solids and Structures 39:41–63

Cardona A (1995) Flexible three dimensional gear modelling. European journal of computational mechanics 4(5-6):663–691

Chen Qz, Acary V, Virlez G, Brüls O (2012) A Newmark-type integrator for flexible systems considering nonsmooth unilateral constraints. In: Proceedings of The Second Joint International Conference on Multibody System Dynamics, May 29-June 1, 2012, Stuttgart, Germany

Chung J, Hulbert G (1993) A time integration algorithm for structural dynamics with improved numerical dissipation: The generalized-α method. ASME Journal of Applied Mechanics 60:371–375

Dumont Y, Paoli L (2008) Numerical simulation of a model of vibrations with joint clearance. International Journal of Computer Applications in Technology 33:41–53

Flores P (2010) A parametric study on the dynamic response of planar multibody systems with multiple clearance joints. nonlin 61:633–653

Flores P, Remco L, Glocker C (2009) Modeling and analysis of planar rigid multibody systems with translational clearance joints based on the non-smooth dynamics approach. msd 23:165–190

Flores P, Machado M, Silva MT, Martins JM (2011) On the continuous contact force models for soft materials in multibody dynamics. Multibody System Dynamics 25:357–375

Géradin M, Cardona A (2001) Flexible multibody dynamics: A finite element approach. John Wiley & Sons, New York

Lankarani H (1988) Canonical equations of motion and estimation of parameters in the analysis of impact problems. PhD thesis, University of Arizona, USA

Lankarani H, Nikravesh P (1994) Continuous contact force models for impact analysis in multibody analysis. Nonlinear Dynamics 5:193–207

Puttock MJ, Thwaite EG (1969) Elastic compression of spheres and cylinders at point and line contact. Research Report 25, Commonwealth Scientific and Industrial Research Organization, Australia

Ravn P (1998) A continuous analysis method for planar multibody systems with joint clearance. msd 2:1–24

Virlez G, Brüls O, Poulet N, Duysinx P (2011) Simulation of differentials in four-wheel drive vehicles using multibody dynamics. In: Proceedings of the ASME 2011 International Design Engineering Technical Conferences Computers and Information in Engineering Conference IDETC/CIE 2011, August 29-31, 2011, Washington, DC, USA